

A new efficient ab-initio approach for calculating the bending stiffness of 2D materials

Farzad Shirazian^a and Roger A. Sauer^{a,b,c,*}

^a*Aachen Institute for Advanced Study in Computational Engineering Science (AICES),
RWTH Aachen University, Templergraben 55, 52056 Aachen, Germany*

^b*Faculty of Civil and Environmental Engineering, Gdańsk University of Technology,
ul. Narutowicza 11/12, 80-233 Gdańsk, Poland*

^c*Dept. of Mechanical Engineering, Indian Institute of Technology Guwahati, Assam 781039, India*

Abstract: This work proposes a new efficient approach for calculating the bending stiffness of two-dimensional materials using simple atomistic tests on small periodic unit cells. The tests are designed such that bending deformations are dominating and membrane deformations are minimized. Atomistic ab-initio simulations then allow for the efficient computation of bending energies. Density functional theory is used for this. Atomistic bending energies are then compared to classical models from structural mechanics. Two different models are considered for this – one based on beam theory and one based on rigid linkage theory – and their results are compared with each other. Four different materials with 2D hexagonal (honeycomb) structure are chosen as a case study: graphene, hexagonal boron nitride, silicene, and blue phosphorene. The calculated bending stiffnesses converge with increasing unit cell size, such that small unit cells already provide accurate results that are in good agreement with the literature. Using the same atomistic tests, it is shown that the bending stiffness of graphene can still be considered constant at moderately large deformations. Apart from being efficient and accurate, the proposed approach allows for various extensions.

Keywords: Bending stiffness, material modeling, graphene, density functional theory, 2D materials

1 Introduction

The discovery of graphene and its successful synthesis (Novoselov et al., 2005) has led researchers to embark on extensive research on two-dimensional materials. These materials exhibit unique properties such as high carrier mobility (Mir et al., 2020), piezoelectricity (Hinchet et al., 2018; Mortazavi et al., 2021), tunable plasmons (Grigorenko et al., 2012; García de Abajo, 2014), quantum Hall effect (Goerbig, 2011), and negative Poisson ratio (Wang et al., 2017a). Depending on test conditions, the Poisson ratio of graphene has been reported positive (Gui et al., 2008) and negative (Jiang et al., 2016; Burmistrov et al., 2018; Jin et al., 2020), which can be attributed to wrinkling caused by defects (Grima et al., 2015) or stresses (Burmistrov et al., 2018). Over the past decade, many more two-dimensional materials with interesting properties have been discovered and studied (Wang et al., 2012; Jiang and Park, 2014; Akinwande et al., 2017; Zhang et al., 2017; Yang et al., 2017; Wang et al., 2017b; Sorokin and Yakobson, 2021; Tong et al., 2021). A criterion for the existence and stability of 2D materials is given in Chen et al. (2017).

Theoretical and computational continuum models developed for these materials play an essential role in the study and design of nanostructures since they allow to study structures at larger

*corresponding author, email: roger.sauer@pg.edu.pl, sauer@aices.rwth-aachen.de

time and length scales than what is practical using atomistic methods. Continuum models require accurate material parameters that need to be determined from ab-initio simulations (Arroyo and Belytschko, 2004; Kumar and Parks, 2015; Ghaffari et al., 2018, 2019; Shirazian et al., 2018). With proper calibration, continuum models allow to describe graphene across a large range of deformations, as a recent comparison has shown (Mokhalingam et al., 2020). Curved two-dimensional materials are especially of interest due to their structural stiffness (Pini et al., 2016) and tunability (Yu et al., 2016), and they serve as a building block for nanostructures such as nanotubes and nanocones. Two-dimensional materials exhibit curvature-dependent bending Poisson effect (Liu et al., 2014), and even a negative bending Poisson ratio has been reported for C3N (Chen et al., 2020). Bending stiffness is an essential parameter to describe the behavior of 2D materials. Two atomistic approaches for the calculation of the bending stiffness of 2D materials are commonly used: (i) computing the bending energy of nanotubes of different radii (Muñoz et al., 2010) and (ii) applying curvature or indentation increments to a large surface with free edges (Scarpa et al., 2010). In the first case, simulations can be very expensive, especially for the study of small curvatures, since more atoms are required to generate nanotubes with small curvatures (i.e. large radii). In the second case, a large supercell has to be used, and the effects of free boundaries need to be dealt with. As a result, both approaches are not ideal for accurate but expensive methods such as density functional theory (DFT), whose simulation cost scales as $O(N^3)$ with the number of atoms (Sholl and Steckel, 2011).

Therefore, a new approach to this problem is proposed here that applies small curvatures to small unit cells with periodic boundary conditions. The approach is efficient, free of boundary effects, characterized by smooth deformations, and applies to all 2D lattice materials. One of the challenges of developing continuum models from atomistic data is establishing a link between the continuous nature of the continuum model and the discreteness of the atomistic unit cell. In order to address this, two different structural models for the analysis of the atomistic tests are suggested and compared. In order to validate each model, the consistency and convergence of the results among different atomic configurations are assessed.

The proposed framework can be used for the calculation of the bending modulus of two-dimensional materials based on atomistic ab-initio simulations that

- require few atoms, making ab-initio simulations efficient;
- are periodic along the in-plane directions, which eliminates free boundary effects;
- are dominated by bending, i.e., membrane energies are negligible; and
- are suitable for the study of a large range of curvatures.

The resulting continuum bending models can then be used to study 2D materials under arbitrary and non-uniform bending conditions.

The remainder of this section presents a review of existing research related to this work. The design of atomistic tests and the details of DFT simulations are elucidated in Secs. 2.1 and 2.2, respectively. In order to develop the continuum bending models, two approaches, a beam (Sec. 2.3) and a rigid linkage (Sec. 2.4) model, are presented for the bending analysis and calibration of its model parameters. In Sec. 3, the presented approach is then used for the determination of bending stiffnesses for graphene (at small and large deformation), hexagonal boron nitride (h-BN), silicene, and blue phosphorene (β -P). This is followed by a detailed discussion in Sec. 4 for each considered case. The paper concludes with Sec. 5.

1.1 Related works

[Berinskii et al. \(2014\)](#) suggest modeling all the carbon bonds using elastic rods. The bending stiffness of graphene is then analytically estimated from the stiffness of the rods. However, Bernoulli-Euler beam theory in this framework does not lead to satisfactory results for graphene, and Timoshenko beam theory requires the determination of too many parameters. Unlike our approach, they consider cross sections, and effectively a thickness for the rods, and determine the properties of the rods from graphene’s elastic parameters instead of atomistic bending tests. In [Zhang et al. \(2011\)](#) and [Nikiforov et al. \(2014\)](#), the authors argue that the bending stiffness of graphene cannot be plausibly defined from 3D elasticity theory, but should be attributed to the torsional misalignment of the π hybrid orbitals. This implies that continuum methods are not sufficient for determining the bending stiffness of 2D materials.

An alternative to continuum methods are atomistic methods based on interatomic potentials. [Arroyo and Belytschko \(2004\)](#) calculate the bending modulus of graphene from bond-order interatomic potentials while characterizing the deformation using the exponential Cauchy-Born rule. [Zhang and Jiang \(2015\)](#) analytically derive the elastic bending stiffness of single-layer black phosphorene from the atomic interactions described by the valence force field model. [Davini et al. \(2017\)](#) determine an equivalent plate equation for the deformations of graphene and use the 2nd-generation Brenner potential to calculate the bending stiffness and the Gaussian stiffness of graphene. As a result, an analytical expression of the Gaussian stiffness is provided. The thermomechanics of monolayer graphene and its out-of-plane thermal fluctuations are studied in [Gao and Huang \(2014\)](#), and the results from harmonic statistical mechanics are compared with NPT and NVT molecular dynamics simulations. The comparison shows the importance of anharmonic effects, especially at higher temperatures and for larger membranes. Considering these effects, [Ahmadpoor et al. \(2017\)](#) study the influence of thermal fluctuations on the bending stiffness and suggest a size-dependent effective bending stiffness for finite temperature using variational perturbation theory.

Although interatomic potentials can provide good results, they are still only approximations of the complex quantum mechanical interactions and can become inaccurate, especially if they are used outside the range they have been designed for. To avoid such inaccuracies, ab-initio atomistic methods, such as DFT, should be used. [Wei et al. \(2013\)](#) use DFT simulations to calculate the bending stiffness of graphene from the energy of single-walled carbon nanotubes of different radii and use this value along with the energies of fullerenes of different sizes to determine the Gaussian bending stiffness of graphene. [Koskinen and Kit \(2010a,b\)](#) suggest to approximate the bending stiffness of two-dimensional materials by extending Bloch’s theorem for curved surfaces, which is very effective for different types of low curvature distortions. Implementing their so-called revised periodic boundary conditions is, however, not straightforward in plane-wave DFT codes ([Kit et al., 2011](#)) and density functional tight binding or classical methods need to be used instead. [Banerjee and Suryanarayana \(2016\)](#) introduce a new method called cyclic density functional theory and develop a symmetry-adapted finite-difference method, which enables the study of cyclic symmetries using Kohn-Sham density functional theory. The application of this method to group-IV nanotubes and forty-four atomic monolayers in the low-curvature limit is presented in [Ghosh et al. \(2019\)](#) and [Kumar and Suryanarayana \(2020\)](#), respectively. These approaches apply the curvature to the unit cell, and, in contrast to our work, the curvature is not directly applied to the atomic configurations.

In addition to the mentioned approaches, the bending stiffness of two-dimensional materials can be determined experimentally through electrostatic actuation ([Lindhahl et al., 2012](#)), folding tests ([Zhao et al., 2015](#)), suspended indentation tests ([Chandler and Vella, 2020](#)), or deformation over a step ([Han et al., 2020](#)), to name a few methods.

2 Methods

2.1 Atomistic bending tests

In order to determine the bending stiffness from ab-initio data, atomistic tests are designed that cause uniaxial bending by applying the displacement w_0 to selected atoms, see Fig. 1. The test configurations are periodic in all directions, and they are designed such that the curvature can be arbitrarily low. As the figure shows, different atomic configurations can be considered: here, all possible periodic atomic configurations with up to 16 distinct atomic positions along the bending direction, which corresponds to the x -direction in Fig. 1. Considering different configurations allows for validating results by comparison. Ideally, the bending stiffness should be independent of the atomic configuration.

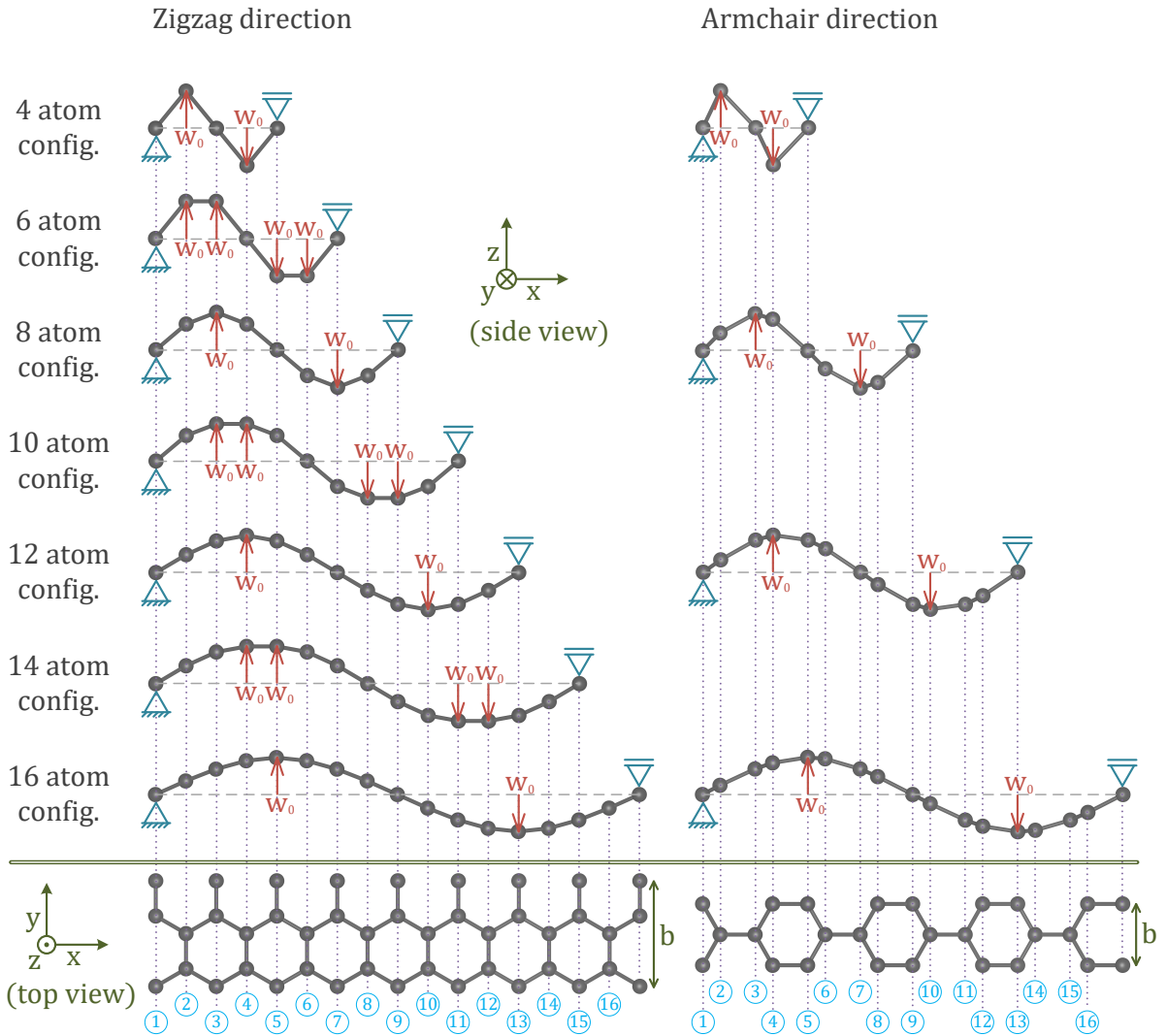


Figure 1: Atomistic bending tests: atomic deflections and boundary conditions for 11 different atomistic test configurations. A predefined out-of-plane displacement w_0 is applied to certain atomic sites, as shown. The boundary atoms are fixed as shown. The rest of the atoms are allowed to relax. The configuration number N is defined as the number of distinct atomic coordinates (visible atoms in the side view), along the x -direction in each unit cell. Therefore, $N = \frac{1}{2} \times (\text{number of atoms})$ for the zigzag and $N = (\text{number of atoms})$ for the armchair direction. The atomic sites are numbered in blue.

It can be seen that the largest unit cell in our proposed framework has 32 atoms, which is still much smaller than the number of atoms required for the classical approach based on nanotubes, especially at small curvatures: for example, the number of atoms for a nanotube unit cell with a curvature of 0.01 nm^{-1} is two orders of magnitude larger than in our proposed approach, which means the quantum mechanical computations for the classical approach would be up to six orders of magnitude larger than for our approach, as the scaling is $O(N^3)$ (Sholl and Steckel, 2011).

2.2 Atomistic simulations

The atomic configurations shown in Fig. 1 are analyzed with DFT simulations at zero Kelvin using periodic unit cells. Displacement w_0 is increased in small increments to reach its final value. At each step, the unit cell dimensions and positions of free atoms are relaxed. The total energy of the unit cell is then calculated from DFT for the relaxed structure.

The DFT simulations are carried out using the QUANTUM ESPRESSO package (P. Giannozzi et al., 2009, 2017). The Perdew-Burke-Ernzerhof (PBE) exchange-correlation functional (Perdew et al., 1996) is used to approximate the energy, and the effects of non-valence electrons are approximated using the Projected Augmented Wave (PAW) method (Blöchl, 1994). The Brillouin zone integrations are performed using meshes generated by the Monkhorst-Pack scheme (Monkhorst and Pack, 1976). The k-point mesh for the primitive cell of the considered 2D materials and kinetic energy cutoff for the wave functions, respectively, are: $40 \times 40 \times 1$ and 60 Ry (Ry = 13.606 eV) for graphene, $30 \times 30 \times 1$ and 100 Ry for h-BN, $40 \times 40 \times 1$ and 100 Ry for silicene, $40 \times 40 \times 1$ and 80 Ry for blue phosphorene. The k-point meshes are then adjusted for the unit cells of different atomic configurations in Fig. 1. The convergence threshold for the self-consistent field iteration is 10^{-8} Ry. The Coulomb interaction between the periodic replicas in the out-of-plane direction is truncated using the method by Sohler et al. (2017) and allowing a 30-35 r_{Bohr} ($r_{\text{Bohr}} = 0.5292 \text{ \AA}$) vacuum space between the periodic replicas.

The energy, force, and pressure convergence threshold for structural optimization are set to 10^{-8} Ry, 10^{-7} Ry/ r_{Bohr} , and 10 mbar, respectively. The initially undeformed and relaxed configurations of the studied materials are shown in Fig. 2.

2.3 Structural mechanics: Beam model

The first method to calculate the bending stiffness uses beam theory. According to Euler-Bernoulli beam theory for small deformations, the out-of-plane deflection of a beam under uniaxial bending with boundary conditions as shown in Fig. 1 is a piece-wise 3rd order polynomial along x that can be written as

$$w = w(x) = a_3x^3 + a_2x^2 + a_1x + a_0, \quad (1)$$

where a_i are constants. The curvature along the bending direction is given as

$$\kappa = \frac{d^2w}{dx^2} \quad (2)$$

for small deformations. Due to symmetry, it is sufficient to determine this polynomial in the range $0 \leq x \leq L$, where $4L$ is the period, i.e., the length of the unit cell. It is possible to decrease the number of unknowns (a_i) from four to one using the following three boundary conditions:

- $w = 0$ at $x = 0$,

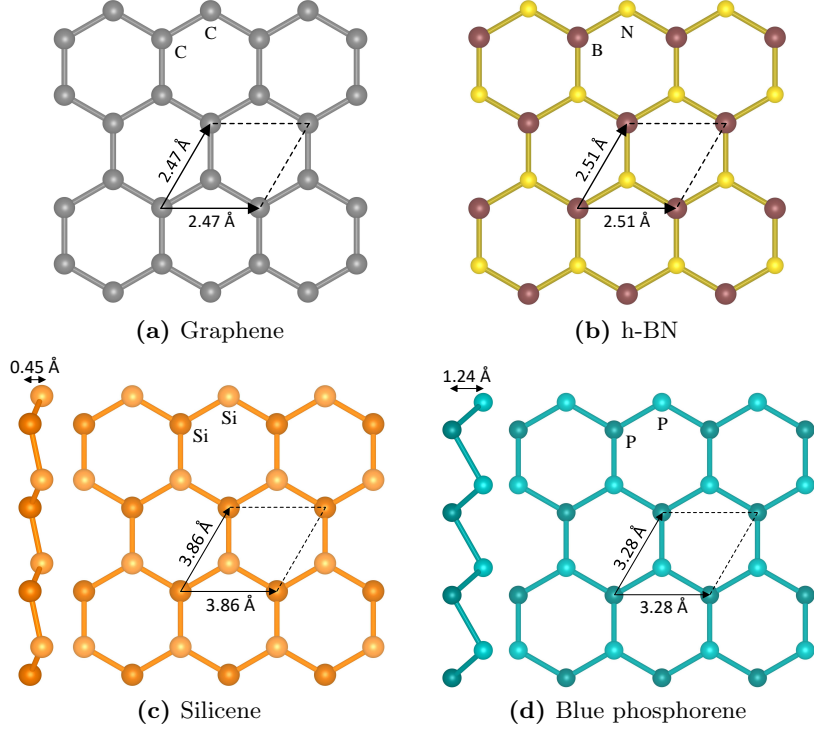


Figure 2: Atomic structure of graphene, hexagonal boron nitride, silicene, and blue phosphorene. The lattice parameters are shown in the figures. Graphene and h-BN are flat, whereas silicene and blue phosphorene have a thickness of 0.45 Å and 1.24 Å, respectively. All atomic structures are visualized with VESTA (Momma and Izumi, 2011).

- $dw/dx = 0$ at $x = L$ to satisfy symmetry and C^1 -continuity of the deflection curve,
- $M = 0$ at $x = 0$, which implies $\kappa = 0$ according to the constitutive relation $M \sim \kappa$.

With this, the deflection and curvature of Eqs. (1) and (2) simplify to

$$w(x) = \alpha \left(3 \frac{x}{L} - \left(\frac{x}{L} \right)^3 \right) \quad (3)$$

and

$$\kappa(x) = -\frac{6\alpha}{L^3}x, \quad (4)$$

where $\alpha := -a_3 L^3$ is proportional to the applied displacement w_0 . α follows from $w(x^*) = w_0$, where x^* denotes the location of the applied displacement w_0 , listed in Tab. 1. Alternatively, α can be determined from minimizing the difference between all atomic positions obtained from DFT and Eq. (3). However, the difference between these alternatives was found to be negligible, which implies that the DFT deflection at the lattice position accurately follows the one predicted by beam theory.

The total strain energy density of a surface can be decomposed as

$$W_{\text{total}} = W_b + W_m, \quad (5)$$

where W_b is bending energy density and W_m is membrane energy density. With the assumption of linear elastic bending behavior, the bending energy density of a sheet bent in one direction

Table 1: Values of $\hat{x} := x^*/L$, determining the location where w_0 is applied, and ξ , determining the energy in the rigid linkage model, for the 11 considered atomic configurations of Fig. 1. The beam deflection follows from Eq. (3) with $\alpha = w_0/(3\hat{x} - \hat{x}^3)$. Note that the values of \hat{x} and ξ depend on the atomic lattice structure, and the listed values correspond to 2D materials with hexagonal (honeycomb) structures.

	Zigzag direction		Armchair direction	
	\hat{x}	ξ	\hat{x}	ξ
4-atom-config.	1	4	2/3	5.6250
6-atom-config.	2/3	4.5		
8-atom-config.	1	8/3	1	2.9460
10-atom-config.	4/5	2.5		
12-atom-config.	1	1.8945	8/9	1.9191
14-atom-config.	6/7	1.7505		
16-atom-config.	1	1.4545	1	1.4400

is given by

$$W_b = \frac{c}{2} \kappa^2, \quad (6)$$

where c is the bending stiffness and κ is the curvature along the bending direction. Based on (4) and (6), the total bending energy of the unit cell, therefore, follows as

$$E_{\text{beam}} = 4b \int_0^L \frac{c}{2} \kappa^2 dx = \frac{24cb\alpha^2}{L^3}. \quad (7)$$

The preceding equations have been derived under the assumption of small deformations. A modified beam model suitable for larger deformations is presented in [Appendix A](#).

2.4 Structural mechanics: Rigid linkage model

Fig. 3 shows the electron density of graphene along its bonds in the deformed zigzag 4-atom-configuration. The deformation resembles that of a rigid linkage – a system of rigid rods connected by hinges and rotational springs, as shown in Fig. 4. The second method for calculating the bending stiffness thus uses rigid linkage theory. In such a system, the rods (bonds) do not contribute to bending, and the bending energy is exclusively stored in the rotational springs (around the atoms), where the angle changes between the rods (bonds) occur. This assumption is valid for most cases. However, in some rare cases, the electron density of the C-C bond does not resemble a straight line ([Wiberg, 1996](#); [Doedens et al., 2017](#)).

In the linear regime, the energy stored in a rotational spring is given by

$$U_s = \frac{k_s b}{2} \theta^2, \quad (8)$$

where the constant k_s is the rotational spring stiffness per width of the unit cell b , and θ is the rotation angle calculated from the current relaxed position of the adjacent atoms. The total

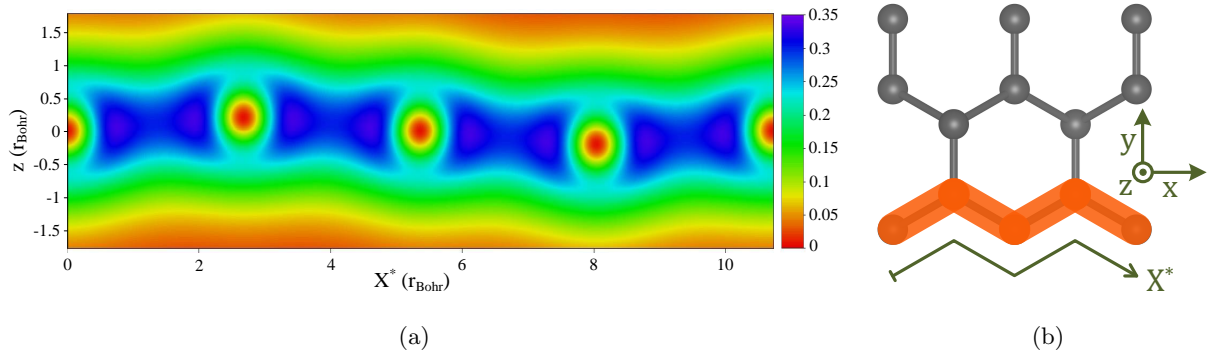


Figure 3: Electron charge density (electron/ r_{Bohr}^3) of the 4-atom-configuration. The charge density is plotted in (a) along the path shown in (b). Bending along the zigzag direction is shown, which is obtained by applying the out-of-plane displacement $w_0 = 0.207 r_{\text{Bohr}}$ to every second atom, as shown in Fig. 1. Plot (a) shows that the atomistic deformation of the surface resembles that of a rigid linkage.

rotational spring energy of a unit cell consisting of n atoms then becomes

$$E_{\text{linkage}} = \frac{k_s b}{2} \sum_{i=1}^n \theta_i^2, \quad (9)$$

where θ_i denote all the angles between the linkages as shown in Fig. 4. These angles can be taken directly from DFT. Alternatively, they can be determined analytically for a given w_0 by calculating the atomic displacements w_i of all the free atoms (atoms 2, 4, 6, and 8 in Fig. 4) from the condition that their force $F_i := \partial E_{\text{linkage}} / \partial w_i$ vanishes. Substituting the obtained result for all θ_i back into Eq. (9), while assuming small deformations ($\tan \theta \approx \theta$), then gives

$$E_{\text{linkage}} = \frac{k_s b \xi}{L^2} w_0^2, \quad (10)$$

where ξ is a constant for each atomic configuration listed in Tab. 1.

As discussed below, k_s is calibrated from atomistic data. Once this is done, Eq. (9) or (10) can be used to calculate the energy of the deformed linkage. Since the spring constant k_s is not the same as the bending stiffness c of the continuum model, the relation between k_s and c is needed in order to determine c from the linkage model. As shown in Appendix B, the equivalent bending stiffness associated with the rotational spring stiffness of the rigid linkage model is

$$c = k_s \bar{a}, \quad (11)$$

where \bar{a} is the average spacing between adjacent atoms that can be calculated by dividing $4L$ by the atomic configuration number. With this, the energies of the unit cells given in Eqs. (9) and (10) become

$$E_{\text{linkage}} = \frac{b c}{2 \bar{a}} \sum_{i=1}^n \theta_i^2 \quad (12)$$

in general, and

$$E_{\text{linkage}} = \frac{b c \xi}{\bar{a} L^2} w_0^2 \quad (13)$$

for infinitesimal strains.

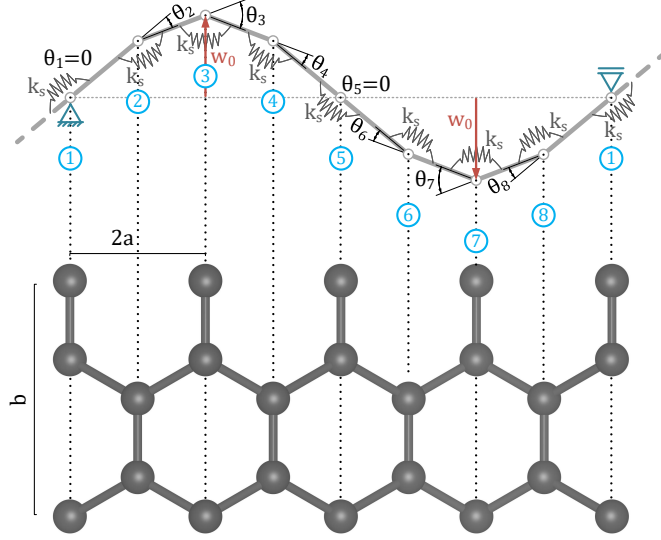


Figure 4: Rigid linkage model for the 8-atom-configuration along the zigzag direction. The atomic sites are numbered in blue. For each atom i , θ_i denotes the out-of-plane component of the bond angle change, which is the relevant component for bending. The in-plane component is not needed, but it can be calculated from θ_i , if desired.

2.5 Calculation of the bending stiffness

In a relaxed unit cell with the described loading conditions, the membrane energies are negligible at small deformations, which is confirmed by the following results. Therefore, according to Eq. (5), the total energy from the DFT calculations corresponds to bending energy. The bending stiffness c can then be calculated from the DFT data by minimizing the cost function

$$C_2(c) = \sum_{k=1}^{N_p} \left(E_{\text{model}}^{(k)}(c) - E_{\text{DFT}}^{(k)} \right)^2, \quad (14)$$

where k denotes the load increment, N_p is the total number of load increments for each atomic configuration, $E_{\text{DFT}}^{(k)}$ are the energies from DFT calculations, and $E_{\text{model}}^{(k)}$ are the energies of the unit cell predicted by either Eq. (7) for the beam model, or Eqs. (12) and (13) for the rigid linkage model. The minimization of the cost function (14) results in one value for the bending stiffness for each atomic configuration.

3 Results

This section presents the results for the bending stiffness from different atomic configurations. First, graphene in the small deformation regime is examined (Sec. 3.1). This is followed by graphene at moderately large deformations (Sec. 3.2). Finally, h-BN, silicene, and blue phosphorene in the small deformation regime are examined (Sec. 3.3). The new results are compared with existing results from the literature.

Small deformations are ensured by picking an average curvature that is at least 100 times smaller than the inverse of the lattice parameter ($\bar{\kappa} < 0.01/a$). For the considered moderately large deformations, on the other hand, the average curvature can be as large as 2 times the inverse lattice parameter ($\bar{\kappa} < 0.5/a$). In all cases the loading was found to be reversible, implying that the material behavior is elastic in the studied ranges.

Table 2: Bending stiffness [nN.nm] of graphene according to the beam and linkage model using the different atomic configurations from Fig. 1. The values can be expected more accurate the larger the unit cell, and more accurate for the linkage model. Existing values from the literature are also shown.

Unit cell	Zigzag direction		Armchair direction	
	Beam model	Linkage model	Beam model	Linkage model
4-atom-config.	0.1512	0.2268	0.1308	0.1923
6-atom-config.	0.2007	0.2459		
8-atom-config.	0.2165	0.2436	0.2217	0.2257
10-atom-config.	0.2244	0.2418		
12-atom-config.	0.2289	0.2417	0.2284	0.2468
14-atom-config.	0.2321	0.2411		
16-atom-config.	0.2331	0.2405	0.2343	0.2441
Other works		Zigzag	No distinction	Armchair
Kudin et al. (2001)			0.2385	
Lu et al. (2009)			0.225	
Wei et al. (2013)			0.231	
Kumar and Suryanarayana (2020)		0.2419		0.2403

3.1 Calibration and validation for graphene at small bending deformations

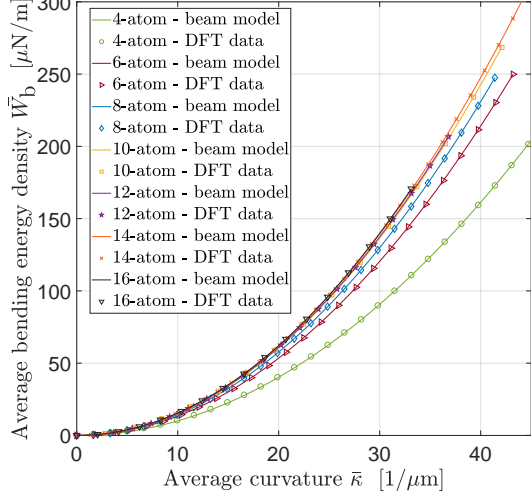
Fig. 5 shows the DFT results for the average bending energy density of the unit cell – i.e., the bending energy divided by the surface area – together with the corresponding results for the calibrated beam and linkage models. The results are presented as a function of the average curvature $\bar{\kappa}$ and average angle change $\bar{\theta}$, respectively, for both the zigzag and the armchair directions. The averages $\bar{\kappa}$ and $\bar{\theta}$ are defined in Appendix C. The calculated bending stiffnesses from the calibrated models are shown in Tab. 2, together with reference results. In order to calculate the bending stiffnesses for the linkage model, first, the spring constants are calculated and then translated to bending stiffnesses using Eq. (11).

3.2 Graphene at moderately large bending deformations

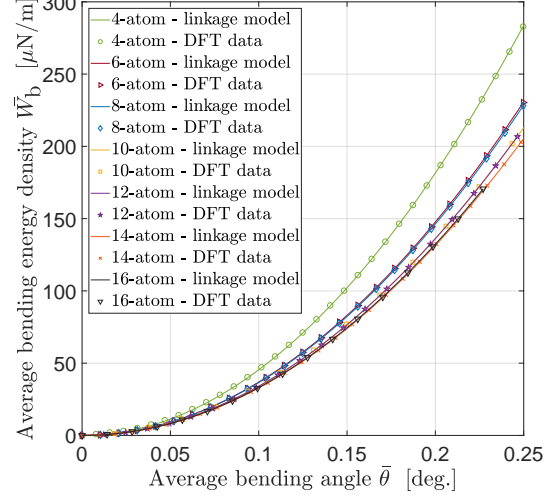
For the calibration of the bending stiffness based on the models presented above, it is necessary to apply infinitesimal strains. At large deformations, however, the bending stiffness is generally no longer constant, such that these models can become inaccurate. In order to investigate how this affects graphene, we assess the performance of the calibrated bending models of Tab. 2 for moderately large deformations. The 8-atom zigzag and 16-atom armchair configurations are considered here, and the applied curvatures are almost two orders of magnitude larger than for the small deformation cases of Tab. 2. The results are presented in Fig. 6. In both tests, it was observed that graphene expands along the y -direction as a result of bending.

In order to accurately calculate the bending energies for larger deformations, some of the simplifications for infinitesimal deformations need to be reconsidered. Eqs. (7) and (13) have been developed for infinitesimal strains for the beam and linkage models, respectively. Therefore, they are not suitable for the calculation of the bending energy when atomistic deformations are moderately large. For the beam model, the energy can be evaluated more accurately if the exact curvature expression is used, as discussed in Appendix A. For the rigid linkage model, the more general expressions (9) and (12), which are not restricted to small deformations, have to be used instead of (10) and (13). Additionally, Eq. (12) should now be evaluated by accounting for the length changes in L and b , obtained from the DFT calculations.

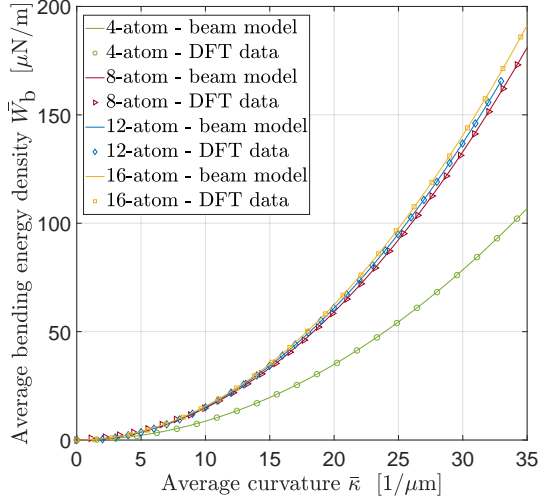
Another aspect that needs to be considered at large deformations is the contribution of the



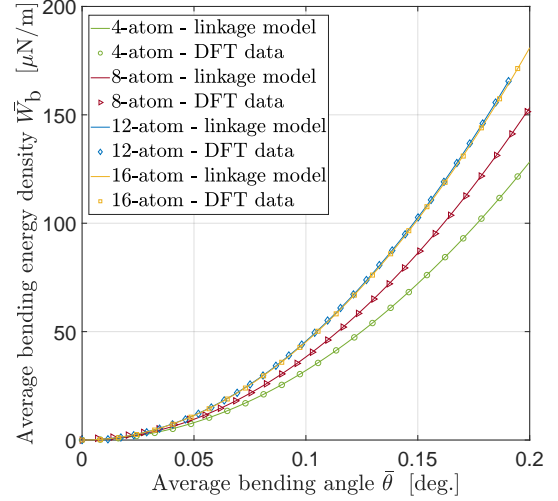
(a) Bending calibration in the zigzag direction using the beam model



(b) Bending calibration in the zigzag direction using the rigid linkage model



(c) Bending calibration in the armchair direction using the beam model



(d) Bending calibration in the armchair direction using the rigid linkage model

Figure 5: Atomistic data and calibrated bending models for graphene at small deformations. As seen, the proposed models describe the atomistic bending behavior very well. The plots show the average bending energy density versus the average curvature $\bar{\kappa}$ for the beam model in (a) and (c), and versus the average bending angle $\bar{\theta}$ for the rigid linkage model in (b) and (d). The DFT data in (a) and (b) as well as in (c) and (d) are the same, respectively. It is just plotted versus the different kinematic quantities ($\bar{\kappa}$ and $\bar{\theta}$) of the two models.

membrane strain energy to the total energy, even though the atomistic tests are designed to minimize this energy. The calculation of the membrane energy at each load increment based on the linkage model is discussed in [Appendix D](#). The calculated membrane energies are also shown in [Fig. 6](#).

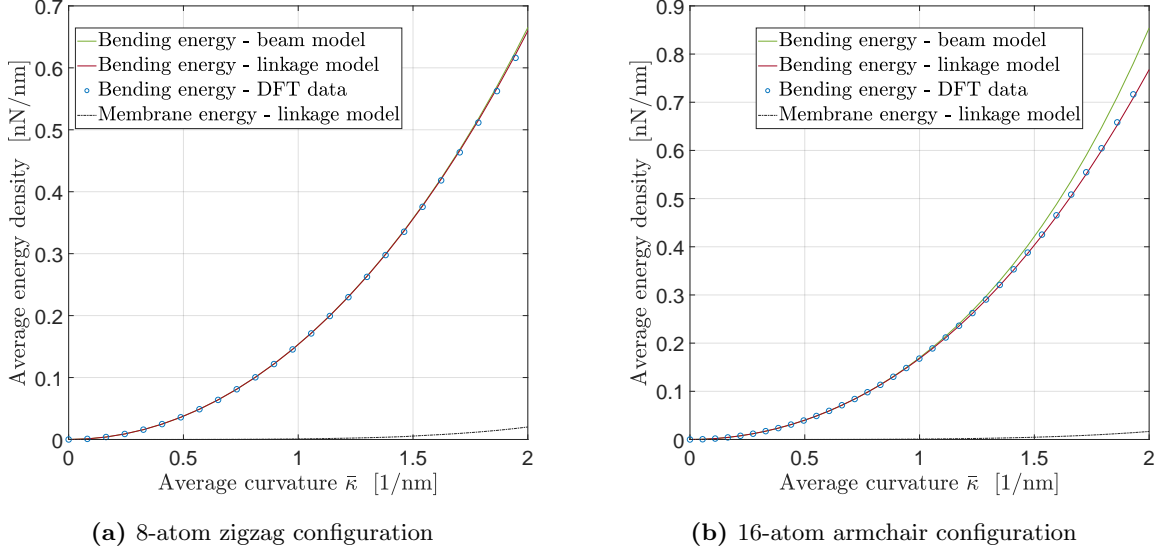
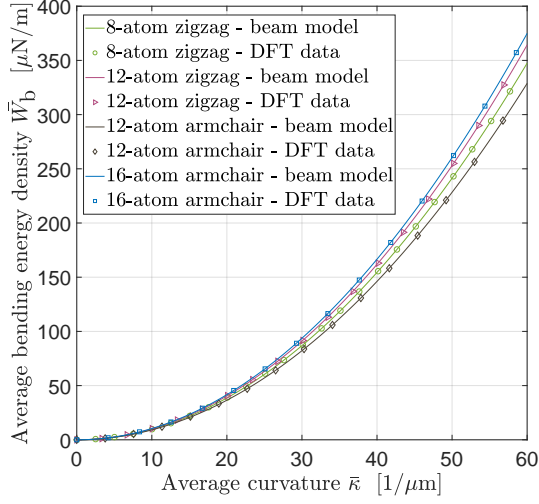


Figure 6: Beam and linkage models for graphene at moderately large deformations. Shown are the 8-atom zigzag and 16-atom armchair configuration. As seen, the proposed calibration still works very well. This is because the membrane energies are still negligible compared to the bending energies, demonstrating that the problem is still bending dominated at these moderately large curvatures.

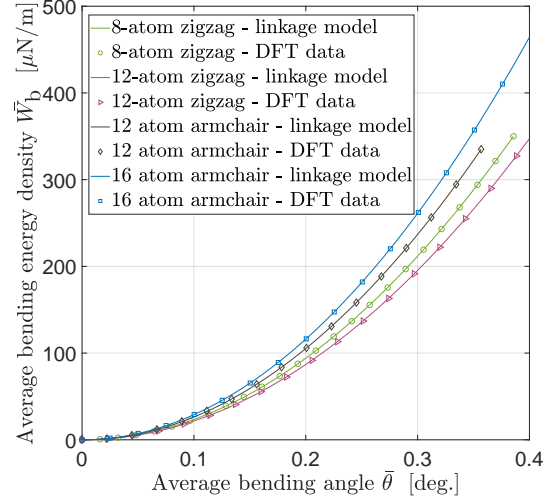
3.3 Application to other 2D materials

The proposed approach can also be used to calculate the bending stiffness for other 2D materials. This is demonstrated on hexagonal boron-nitride (h-BN), silicene, and blue phosphorene. [Fig. 7](#) shows their bending calibration along the zigzag and armchair directions. For the zigzag direction, the 8- and 12-atom-configurations, and for the armchair direction, the 12- and 16-atom-configurations are considered.

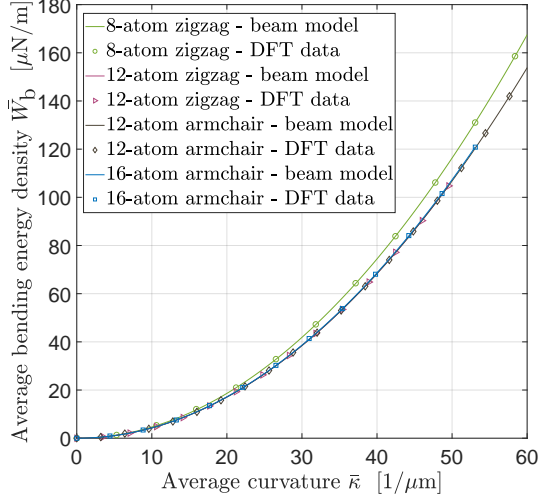
The determined values for the bending stiffness of h-BN, silicene, and blue phosphorene are listed in [Tab. 3](#), along with the already determined value of graphene at small deformations and known values from the literature. The reported bending stiffnesses for graphene correspond to the 16-atom-configurations along the zigzag and armchair directions from [Tab. 2](#). For h-BN, silicene, and blue phosphorene, the reported values correspond to the 12-atom-configurations along the zigzag direction and the 16-atom-configurations along the armchair direction. The values of the bending stiffness are reported separately for each atomic configuration in [Tab. E.1](#). One additional parameter of corrugated lattices such as silicene and blue phosphorene in comparison to flat ones such as graphene and h-BN is their initial thickness. This is accounted for in our approach by applying the displacement w_0 directly to the initial position of the atoms. This is equivalent to assuming w_0 is applied to the midsurface of the corrugated material and further assuming that lateral displacements of non-midsurface atoms as well as thickness changes are negligible during deformation, which is reasonable for small deformations.



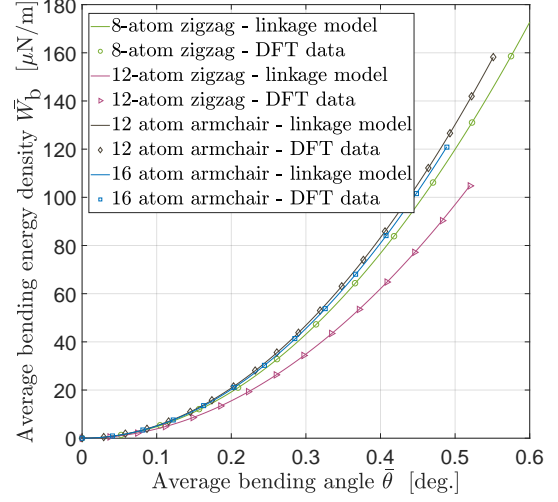
(a) Calibration of h-BN from the beam model



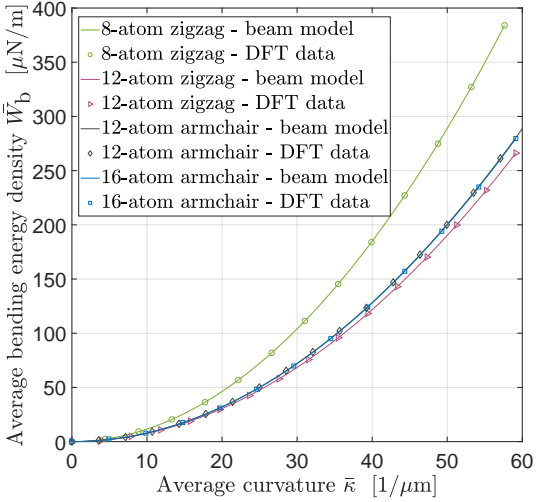
(b) Calibration of h-BN from the linkage model



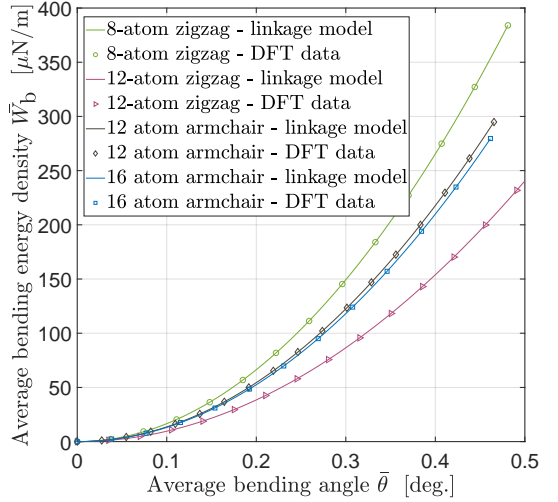
(c) Calibration of silicene from the beam model



(d) Calibration of silicene from the linkage model



(e) Calibration of blue P from the beam model



(f) Calibration of blue P from the linkage model

Figure 7: Atomistic data and calibrated models for hexagonal boron nitride, silicene, and blue phosphorene at small deformations. Left side: beam model calibration. Right side: linkage model calibration. Again, the proposed models describe the atomistic bending behavior very well. The DFT data in the corresponding left and right figures are the same for each material. It is just plotted versus the different kinematic quantities ($\bar{\kappa}$ and $\bar{\theta}$) of the two models.

Table 3: Calibrated bending stiffnesses [nN.nm] of the investigated 2D materials and their comparison with reference values from the literature, namely **K01** (Kudin et al., 2001), **L09** (Lu et al., 2009), **W13** (Wei et al., 2013), **R14** (Roman and Cranford, 2014), **B16** (Banerjee and Suryanarayana, 2016), **Q19** (Qu et al., 2019), **K20** (Kumar and Suryanarayana, 2020), and **Z20** (Zhang et al., 2020). The calibrated bending stiffnesses are from the largest available unit cell in all cases (see Fig. 7), as it can be expected to give the most accurate values. In the cited literature with only one value, no distinction between zigzag and armchair directions is made. All reference results are based on ab-initio calculations, except the large silicene value of Roman and Cranford (2014), which is based on MD calculations.

		Beam model	Linkage model	Ref. 1	Ref. 2	Ref. 3	Ref. 4
Graphene	Z	0.2331	0.2343	0.2385 (K01)	0.225 (L09)	0.231 (W13)	0.2419 (K20)
	A	0.2405	0.2441				
h-BN	Z	0.1518	0.1602	0.138 (Q19)	0.0897 (K20)	-	-
	A	0.1562	0.1627				
Silicene	Z	0.0641	0.0677	6.184 (R14)	0.986 (B16)	0.0577 (K20)	-
	A	0.0644	0.0671				
Blue phosphorene	Z	0.1142	0.1205	0.1196 (Z20)	-	-	-
	A	0.1199	0.1249				

4 Discussion

4.1 Calibration and validation for graphene at small bending deformations

Fig. 5 shows that graphene is described very accurately at small deformations by both the beam and linkage models, which implies that the proposed methods allow for the accurate determination of the bending stiffness from DFT calculations. This is confirmed by the good agreement with the bending stiffnesses obtained from other approaches in the literature, as Tab. 2 shows. The computational complexity of our proposed approach, however, is generally much lower due to its simplicity and lower number of atoms per unit cell, especially at smaller curvatures.

In addition, Tab. 2 shows that the bending stiffness is captured more accurately from the DFT tests if higher atomic configurations (i.e. bigger units cells) and the linkage model are used. This is due to the following reasons: The localized deformation of graphene is better captured by a discrete linkage model than a continuous beam model. At the same time, the continuous deformation assumption, inherent to the concept of a bending stiffness, is not accurate for lower atomic configurations. The results in Tab. 2 indicate that at least the 12-atom-configuration should be used together with the linkage model to accurately compute the bending stiffness. Moreover, the bending stiffness for the zigzag and armchair directions approach the same value, confirming graphene’s known isotropic bending behavior at small deformations. This, however, does not exclude the possibility that zigzag and armchair bending is coupled, which is an aspect that should be investigated in detail in future work. The fact that the accuracy is poor for lower atomic configurations shows that continuum bending models should be used cautiously for deformations exhibiting very large curvatures, even if those deformations are only local.

4.2 Graphene at moderately large bending deformations

Fig. 6 shows that the bending stiffnesses calibrated from small deformation theory still capture moderately large bending deformation behavior for graphene very well. This demonstrates that even at moderately large curvatures, the bending energy density of graphene still depends

quadratically on the curvature, although now large deformation kinematics should be considered via [Appendix A](#) for the beam model, and Eq. (12) for the linkage model, which is what is done in Fig. 6. Based on this, the bending stiffness is still constant, at least as long as the membrane stresses are negligible. Fig. 6 shows that this is the case in our suggested DFT calibration tests, which is why they allow extracting the bending stiffness reliably in the first place. On the other hand, if membrane stresses are significant, coupling between in-plane stretching and bending can be expected to affect bending, leading to an increase in the effective bending resistance. This increase is well understood in structural mechanics, but it remains to be seen if it exactly carries over to 2D lattice materials.

4.3 Application to other 2D materials

In addition to graphene, the proposed method has been used to calculate the bending stiffness of h-BN, silicene, and blue phosphorene. The results show good agreement with the works of [Qu et al. \(2019\)](#) and [Zhang et al. \(2020\)](#) but disagree with other works ([Roman and Cranford, 2014](#); [Banerjee and Suryanarayana, 2016](#); [Kumar and Suryanarayana, 2020](#)) (although the disagreement with [Kumar and Suryanarayana \(2020\)](#) is quite small for silicene). The large disagreement with [Roman and Cranford \(2014\)](#) can be attributed to the MD calculations used there, whereas the large disagreement with [Banerjee and Suryanarayana \(2016\)](#) can be attributed to their use of a non-relaxed silicene nanoribbon, which entails a size-effect due to the ribbon boundaries. Despite the corrugation of silicene and blue phosphorene, the bending stiffness of graphene and h-BN is higher, as Tab. 3 shows. This implies that (1) the atomic bonds play a more important role in the bending stiffness than the surface geometry, and (2) the atomic bonds of graphene and h-BN provide more resistance to bending than those of silicene and blue phosphorene. The latter point is consistent with the known fact that graphene and h-BN have larger Young's moduli than silicene and blue phosphorene ([Falin et al., 2017](#); [Mortazavi et al., 2017](#); [Ghaffari et al., 2019](#)).

Due to the corrugated structure of silicene and blue phosphorene, the bending stiffness in the zigzag direction might be expected to be higher than the bending stiffness in the armchair direction since the second moment of area appears to be larger for bending along the zigzag direction ([Woodruff and Filipov, 2020](#)). However, the second moment of inertia not only comes from the thickness shown in Fig. 2. More relevant is the effective thickness of the electron clouds, which can be expected to be similar in both directions. Therefore, no significant difference between the armchair and zigzag bending stiffnesses should appear. This is confirmed by our results in Tab. 3. It again shows the small influence of the surface corrugation.

We also note that for very small deformations and energies, computational errors and inherent inaccuracies of DFT might become significant and affect the calculated energies negatively, even though some systematic errors cancel each other when only considering the energy differences in similar unit cells ([Sholl and Steckel, 2011](#)). In the considered infinitesimal regime, however, only results with sufficiently large curvatures have been used to avoid these issues. Moreover, poor choice of DFT convergence parameters can result in wrong bending stiffness values.

5 Conclusion

The suggested framework uses relatively small unit cells, is computationally efficient, and is easy to implement in conventional atomistic simulation codes. Therefore, it can be used for the efficient and accurate determination of continuum bending parameters for two-dimensional materials. The framework is very flexible and hence admits many possible extensions: Examples

are the incorporation of biaxial bending, larger deformations, membrane-bending coupling, and finite temperatures.

Acknowledgements

Funding: This work was initially supported by the German Research Foundation through project GSC 111.

Data availability

All results and representative input files for Quantum Espresso can be provided on request.

A Modified beam model for large deformations

At moderately large deformations, some of the approximations used in the development of the infinitesimal beam model become inaccurate. This section, therefore, presents a more general approach, which is used in the calculation of the energies in Fig. 6.

As a result of bending, the length of the unit cell can change and is now denoted by 4ℓ . Considering this change in the formulation, the deflection of the beam is still assumed to follow Eq. (3). But the curvature is now taken from the exact expression

$$\kappa(x) = \frac{w''}{(1 + (w')^2)^{3/2}}, \quad (\text{A.1})$$

where $w' = dw/dx = 3\alpha(\ell^2 - x^2)/\ell^3$ and $w'' = d^2w/dx^2 = -6\alpha x/\ell^3$. The bending energy of the unit cell can then be calculated along the curve as

$$E_{\text{beam}} = \int_0^S \frac{c}{2} \kappa^2 ds, \quad (\text{A.2})$$

where

$$S = \int_0^S ds = \int_0^\ell \sqrt{1 + (w')^2} dx \quad (\text{A.3})$$

is the length of the deflected beam at each load increment.

B Equivalent bending stiffness in the rigid linkage model

This section derives the equivalent bending stiffness from given spring stiffness k_s in the rigid linkage model. Fig. B.1 shows a segment of the curved atomic surface. Along the armchair direction $a_1 \neq a_2$, while along the zigzag direction $a_1 = a_2$. Assuming that the curvature is constant along $2\bar{a} = a_1 + a_2$, the rotation angle of the spring can be obtained from

$$2r \sin \frac{\gamma_i}{2} = a_i \quad (i = 1, 2) \quad (\text{B.1})$$

and

$$\theta = \frac{\gamma_1}{2} + \frac{\gamma_2}{2} = \arcsin \frac{a_1}{2r} + \arcsin \frac{a_2}{2r} = \arcsin \left(\frac{a_1}{4r^2} \sqrt{4r^2 - a_2^2} + \frac{a_2}{4r^2} \sqrt{4r^2 - a_1^2} \right), \quad (\text{B.2})$$

which can then be used in Eq. (8) to obtain the energy of the spring U_s from the linkage model. The corresponding energy from the continuum model can be calculated as

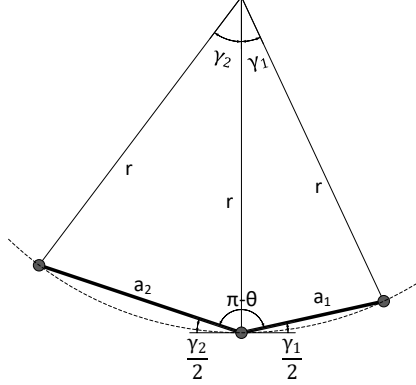


Figure B.1: An equivalent atomic system with constant curvature. The more general armchair direction with $a_1 \neq a_2$ is shown.

$$U_c = \int_{-\frac{\gamma_2}{2}}^{\frac{\gamma_1}{2}} b \frac{c}{2} \kappa^2 ds = b \frac{c}{2} \frac{1}{r^2} r \left(\frac{\gamma_1 + \gamma_2}{2} \right) = \frac{bc}{2r} \theta. \quad (\text{B.3})$$

Setting $U_c = U_s$ gives

$$c = k_s r \arcsin \left(\frac{a_1}{4r^2} \sqrt{4r^2 - a_2^2} + \frac{a_2}{4r^2} \sqrt{4r^2 - a_1^2} \right). \quad (\text{B.4})$$

It can be seen that the bending stiffness generally depends on the bending radius. For small deformations, however, $a_1/r, a_2/r \ll 1$ and $\arcsin(\bar{a}/r) \approx \bar{a}/r$ such that Eq. (B.4) tends to

$$c = k_s \bar{a}. \quad (\text{B.5})$$

Even for large curvatures up to $\bar{a}/r < 0.5$, the difference between (B.4) and (B.5) is less than 1.5%.

C Average curvature, angle, and energy density

This section presents the definition of the three average quantities used in Figs. 5-7. The average curvature is a useful measure to compare different atomic configurations using the beam model, and it is defined at each load increment as

$$\bar{\kappa} := -\frac{1}{S} \int_0^S \kappa(s) ds \approx -\frac{1}{L} \int_0^L \kappa(x) dx = \frac{3\alpha}{L^2}. \quad (\text{C.1})$$

The curvature in $0 \leq x \leq L$ is negative for the deformations of Fig. 1, hence the negative sign is added to make $\bar{\kappa}$ positive. For the rigid linkage model, the average angle change

$$\bar{\theta} := \frac{1}{n} \sum_{i=1}^n \theta_i \quad (\text{C.2})$$

is used for the comparison of different atomic configurations. Under the small deformation assumption, follows

$$\bar{\theta} = \chi \frac{w_0}{\bar{a}}, \quad (\text{C.3})$$

where the values of χ are tabulated in Tab. C.1. Multiplying (C.1) by $1 = \bar{a}\bar{\theta}/(\chi w_0)$, which follows from (C.3), gives the relation between the two average measures,

$$\bar{\kappa} = \frac{3\alpha\bar{a}}{\chi w_0 L^2} \bar{\theta}, \quad (\text{C.4})$$

where α/w_0 is tabulated in Tab. 1.

Table C.1: Values of χ in the rigid linkage model for different atomic configurations

Zigzag direction	χ	Armchair direction	χ
4-atom-config.	1	4-atom-config.	3/2
6-atom-config.	2/3		
8-atom-config.	1/3	8-atom-config.	0.3804
10-atom-config.	6/25		
12-atom-config.	3/19	12-atom-config.	0.1602
14-atom-config.	6/49		
16-atom-config.	1/11	16-atom-config.	0.09

The third quantity, the average energy density, is defined by

$$\bar{W}_\bullet := \frac{E_\bullet}{4Lb}, \quad (\text{C.5})$$

where E_\bullet collectively denotes various cases: the bending energies of the beam (Eqs. (7) and (A.2)) or linkage model (Eqs. (13) and (12)), or the membrane energy from the linkage model (Eq. (D.2)).

D Calculation of membrane energies at large deformations

This section presents the calculation of the membrane strain energy, which is essential for the assessment of large deformations. Since the linkage kinematics in Fig. 4 is not approximate, the linkage model is used for the calculation.

Allowing now for stretchable links, the stretch of the links and the stretch in lateral direction follow as

$$(\lambda_1)_i = \frac{d_i}{(d_0)_i} \quad \lambda_2 = \frac{b}{b_0}, \quad (\text{D.1})$$

where d_i , $(d_0)_i$, b , and b_0 are the current and the initial length of link i , and the current and the initial unit cell width, respectively. They follow from the DFT data. The total membrane energy is the sum of the membrane energies of all links and is then given by

$$\Psi_{\text{linkage}} = b \sum_{i=1}^{N_{\text{links}}} d_i W_m((\lambda_1)_i, \lambda_2), \quad (\text{D.2})$$

where N_{links} is the number of links and W_m is the membrane energy density from a suitable material model, such as the one for graphene presented in (Shirazian et al., 2018).

E Bending stiffness values of h-BN, silicene, and blue phosphorene for different atomic configurations

The bending stiffnesses of h-BN, silicene, and blue phosphorene have been calculated for the 8- and 12-atom configurations along the zigzag, and 12- and 16-atom configurations along the armchair direction. The values for the beam and linkage model are given in Tab. E.1.

Table E.1: The calibrated bending stiffness c [nN.nm] for different atomic configurations of h-BN, silicene, and blue phosphorene.

	h-BN	Silicene	Blue phosphorene
8-atom-config. zigzag — beam model	0.1448	0.0698	0.1734
8-atom-config. zigzag — linkage model	0.1629	0.0785	0.1950
12-atom-config. zigzag — beam model	0.1518	0.0641	0.1142
12-atom-config. zigzag — linkage model	0.1602	0.0677	0.1205
12-atom-config. armchair — beam model	0.1370	0.0641	0.1203
12-atom-config. armchair — linkage model	0.1480	0.0692	0.1300
16-atom-config. armchair — beam model	0.1562	0.0644	0.1199
16-atom-config. armchair — linkage model	0.1627	0.0671	0.1249

References

- Ahmadpoor, F., Wang, P., Huang, R., and Sharma, P. (2017). Thermal fluctuations and effective bending stiffness of elastic thin sheets and graphene: A nonlinear analysis. *J. Mech. Phys. Solids*, **107**:294–319.
- Akinwande, D., Brennan, C. J., Bunch, J. S., Egberts, P., Felts, J. R., Gao, H., Huang, R., Kim, J.-S., Li, T., Li, Y., Liechti, K. M., Lu, N., Park, H. S., Reed, E. J., Wang, P., Yakobson, B. I., Zhang, T., Zhang, Y.-W., Zhou, Y., and Zhu, Y. (2017). A review on mechanics and mechanical properties of 2d materials—graphene and beyond. *Extreme Mech. Lett.*, **13**:42 – 77.
- Arroyo, M. and Belytschko, T. (2004). Finite crystal elasticity of carbon nanotubes based on the exponential Cauchy-Born rule. *Phys. Rev. B*, **69**(11):115415.
- Banerjee, A. S. and Suryanarayana, P. (2016). Cyclic density functional theory: A route to the first principles simulation of bending in nanostructures. *J. Mech. Phys. Solids*, **96**:605–631.
- Berinskii, I. E., Krivtsov, A. M., and Kudarova, A. M. (2014). Bending stiffness of a graphene sheet. *Phys. Mesomech.*, **17**(4):356–364.
- Blöchl, P. E. (1994). Projector augmented-wave method. *Phys. Rev. B*, **50**(24):17953–17979.
- Burmistrov, I. S., Gornyi, I. V., Kachorovskii, V. Y., Katsnelson, M. I., Los, J. H., and Mirlin, A. D. (2018). Stress-controlled Poisson ratio of a crystalline membrane: Application to graphene. *Phys. Rev. B*, **97**(12):125402.

- Chandler, T. and Vella, D. (2020). Indentation of suspended two-dimensional solids: The signatures of geometrical and material nonlinearity. *J. Mech. Phys. Solids*, **144**:104109.
- Chen, J., Wang, B., and Hu, Y. (2017). An existence criterion for low-dimensional materials. *J. Mech. Phys. Solids*, **107**:451–468.
- Chen, Z., Wang, H., and Li, Z. (2020). First-principles study of two dimensional C3N and its derivatives. *RSC Adv.*, **10**(55):33469–33474.
- Davini, C., Favata, A., and Paroni, R. (2017). The Gaussian stiffness of graphene deduced from a continuum model based on molecular dynamics potentials. *J. Mech. Phys. Solids*, **104**:96–114.
- Doedens, R. J., Eaton, P. E., and Fleischer, E. B. (2017). The bent bonds of cubane. *Eur. J. Org. Chem.*, **2017**(18):2627–2630.
- Falin, A., Cai, Q., Santos, E. J. G., Scullion, D., Qian, D., Zhang, R., Yang, Z., Huang, S., Watanabe, K., Taniguchi, T., Barnett, M. R., Chen, Y., Ruoff, R. S., and Li, L. H. (2017). Mechanical properties of atomically thin boron nitride and the role of interlayer interactions. *Nat. Commun.*, **8**(1):15815.
- Gao, W. and Huang, R. (2014). Thermomechanics of monolayer graphene: Rippling, thermal expansion and elasticity. *J. Mech. Phys. Solids*, **66**:42–58.
- García de Abajo, F. J. (2014). Graphene plasmonics: Challenges and opportunities. *ACS Photonics*, **1**(3):135–152.
- Ghaffari, R., Duong, T. X., and Sauer, R. A. (2018). A new shell formulation for graphene structures based on existing *ab-initio* data. *Int. J. Solids Struct.*, **135**:37–60.
- Ghaffari, R., Shirazian, F., Hu, M., and Sauer, R. A. (2019). A nonlinear hyperelasticity model for single layer blue phosphorus based on *ab initio* calculations. *Proc. R. Soc. A: Math. Phys. Eng. Sci.*, **475**(2229):20190149.
- Ghosh, S., Banerjee, A. S., and Suryanarayana, P. (2019). Symmetry-adapted real-space density functional theory for cylindrical geometries: Application to large group-iv nanotubes. *Phys. Rev. B*, **100**(12):125143.
- Goerbig, M. O. (2011). Electronic properties of graphene in a strong magnetic field. *Rev. Mod. Phys.*, **83**(4):1193–1243.
- Grigorenko, A. N., Polini, M., and Novoselov, K. S. (2012). Graphene plasmonics. *Nat. Photonics*, **6**(11):749–758.
- Grima, J. N., Winczewski, S., Mizzi, L., Grech, M. C., Cauchi, R., Gatt, R., Attard, D., Wojciechowski, K. W., and Rybicki, J. (2015). Tailoring graphene to achieve negative Poisson’s ratio properties. *Adv. Mater.*, **27**(8):1455–1459.
- Gui, G., Li, J., and Zhong, J. (2008). Band structure engineering of graphene by strain: First-principles calculations. *Phys. Rev. B*, **78**(7):075435.
- Han, E., Yu, J., Annevelink, E., Son, J., Kang, D. A., Watanabe, K., Taniguchi, T., Ertekin, E., Huang, P. Y., and van der Zande, A. M. (2020). Ultrasoft slip-mediated bending in few-layer graphene. *Nat. Mater.*, **19**(3):305–309.
- Hinchet, R., Khan, U., Falconi, C., and Kim, S.-W. (2018). Piezoelectric properties in two-dimensional materials: Simulations and experiments. *Mater. Today*, **21**(6):611–630.

- Jiang, J.-W., Chang, T., Guo, X., and Park, H. S. (2016). Intrinsic negative Poisson’s ratio for single-layer graphene. *Nano Lett.*, **16**(8):5286–5290.
- Jiang, J.-W. and Park, H. S. (2014). Negative Poisson’s ratio in single-layer black phosphorus. *Nat. Commun.*, **5**(1):4727.
- Jin, W., Sun, W., Kuang, X., Lu, C., and Kou, L. (2020). Negative Poisson ratio in two-dimensional tungsten nitride: Synergistic effect from electronic and structural properties. *J. Phys. Chem. Lett.*, **11**(22):9643–9648.
- Kit, O. O., Pastewka, L., and Koskinen, P. (2011). Revised periodic boundary conditions: Fundamentals, electrostatics, and the tight-binding approximation. *Phys. Rev. B*, **84**(15):155431.
- Koskinen, P. and Kit, O. O. (2010a). Approximate modeling of spherical membranes. *Phys. Rev. B*, **82**(23):235420.
- Koskinen, P. and Kit, O. O. (2010b). Efficient approach for simulating distorted materials. *Phys. Rev. Lett.*, **105**(10):106401.
- Kudin, K. N., Scuseria, G. E., and Yakobson, B. I. (2001). C₂F, BN, and C nanoshell elasticity from ab initio computations. *Phys. Rev. B*, **64**(23):235406.
- Kumar, S. and Parks, D. M. (2015). On the hyperelastic softening and elastic instabilities in graphene. *Proc. R. Soc. A: Math. Phys. Eng. Sci.*, **471**(2173):20140567.
- Kumar, S. and Suryanarayana, P. (2020). Bending moduli for forty-four select atomic monolayers from first principles. *Nanotechnology*, **31**(43):43LT01.
- Lindahl, N., Midtvedt, D., Svensson, J., Nerushev, O. A., Lindvall, N., Isacson, A., and Campbell, E. E. B. (2012). Determination of the bending rigidity of graphene via electrostatic actuation of buckled membranes. *Nano Lett.*, **12**(7):3526–3531.
- Liu, X., Pan, D., Hong, Y., and Guo, W. (2014). Bending Poisson effect in two-dimensional crystals. *Phys. Rev. Lett.*, **112**(20):205502.
- Lu, Q., Arroyo, M., and Huang, R. (2009). Elastic bending modulus of monolayer graphene. *J. Phys. D: Appl. Phys.*, **42**(10):102002.
- Mir, S. H., Yadav, V. K., and Singh, J. K. (2020). Recent advances in the carrier mobility of two-dimensional materials: A theoretical perspective. *ACS Omega*, **5**(24):14203–14211.
- Mokhalingam, A., Ghaffari, R., Sauer, R. A., and Gupta, S. S. (2020). Comparing quantum, molecular and continuum models for graphene at large deformations. *Carbon*, **159**:478–494.
- Momma, K. and Izumi, F. (2011). Vesta 3 for three-dimensional visualization of crystal, volumetric and morphology data. *J. Appl. Crystallogr.*, **44**(6):1272–1276.
- Monkhorst, H. J. and Pack, J. D. (1976). Special points for Brillouin-zone integrations. *Phys. Rev. B*, **13**(12):5188–5192.
- Mortazavi, B., Javvaji, B., Shojaei, F., Rabczuk, T., Shapeev, A. V., and Zhuang, X. (2021). Exceptional piezoelectricity, high thermal conductivity and stiffness and promising photocatalysis in two-dimensional MoSi₂N₄ family confirmed by first-principles. *Nano Energy*, **82**:105716.

- Mortazavi, B., Rahaman, O., Makaremi, M., Dianat, A., Cuniberti, G., and Rabczuk, T. (2017). First-principles investigation of mechanical properties of silicene, germanene and stanene. *Phys. E: Low-dimens. Syst. Nanostructures*, **87**:228–232.
- Muñoz, E., Singh, A. K., Ribas, M. A., Penev, E. S., and Yakobson, B. I. (2010). The ultimate diamond slab: Graphane versus graphene. *Diam. Relat. Mater.*, **19**(5):368–373. Proceedings of Diamond 2009, The 20th European Conference on Diamond, Diamond-Like Materials, Carbon Nanotubes and Nitrides, Part 1.
- Nikiforov, I., Dontsova, E., James, R. D., and Dumitrică, T. (2014). Tight-binding theory of graphene bending. *Phys. Rev. B*, **89**(15):155437.
- Novoselov, K. S., Jiang, D., Schedin, F., Booth, T. J., Khotkevich, V. V., Morozov, S. V., and Geim, A. K. (2005). Two-dimensional atomic crystals. *Proc. Natl. Acad. Sci.*, **102**(30):10451–10453.
- P. Giannozzi et. al. (2009). QUANTUM ESPRESSO: a modular and open-source software project for quantum simulations of materials. *J. Phys. Condens. Matter*, **21**(39):395502.
- P. Giannozzi et. al. (2017). Advanced capabilities for materials modelling with quantum ESPRESSO. *J. Phys. Condens. Matter*, **29**(46):465901.
- Perdew, J. P., Burke, K., and Ernzerhof, M. (1996). Generalized gradient approximation made simple. *Phys. Rev. Lett.*, **77**(18):3865–3868.
- Pini, V., Ruz, J. J., Kosaka, P. M., Malvar, O., Calleja, M., and Tamayo, J. (2016). How two-dimensional bending can extraordinarily stiffen thin sheets. *Sci. Rep.*, **6**(1):29627.
- Qu, W., Bagchi, S., Chen, X., Chew, H. B., and Ke, C. (2019). Bending and interlayer shear moduli of ultrathin boron nitride nanosheet. *J. Phys. D: Appl. Phys.*, **52**(46):465301.
- Roman, R. E. and Cranford, S. W. (2014). Mechanical properties of silicene. *Comput. Mater. Sci.*, **82**:50–55.
- Scarpa, F., Adhikari, S., Gil, A. J., and Remillat, C. (2010). The bending of single layer graphene sheets: the lattice versus continuum approach. *Nanotechnology*, **21**(12):125702.
- Shirazian, F., Ghaffari, R., Hu, M., and Sauer, R. A. (2018). Hyperelastic material modeling of graphene based on density functional calculations. *PAMM*, **18**(1):e201800419.
- Sholl, D. and Steckel, J. A. (2011). *Density functional theory: a practical introduction*. John Wiley & Sons.
- Sohier, T., Calandra, M., and Mauri, F. (2017). Density functional perturbation theory for gated two-dimensional heterostructures: Theoretical developments and application to flexural phonons in graphene. *Phys. Rev. B*, **96**(7):075448.
- Sorokin, P. B. and Yakobson, B. I. (2021). Two-dimensional diamond—diamane: Current state and further prospects. *Nano Lett.*, **21**(13):5475–5484.
- Tong, Z., Dumitrică, T., and Frauenheim, T. (2021). Ultralow thermal conductivity in two-dimensional MoO₃. *Nano Lett.*, **21**(10):4351–4356.
- Wang, H., Li, X., Li, P., and Yang, J. (2017a). δ -Phosphorene: a two dimensional material with a highly negative Poisson’s ratio. *Nanoscale*, **9**(2):850–855.

- Wang, H., Li, X., Liu, Z., and Yang, J. (2017b). ψ -Phosphorene: a new allotrope of phosphorene. *Phys. Chem. Chem. Phys.*, **19**(3):2402–2408.
- Wang, Q. H., Kalantar-Zadeh, K., Kis, A., Coleman, J. N., and Strano, M. S. (2012). Electronics and optoelectronics of two-dimensional transition metal dichalcogenides. *Nat. Nanotechnol.*, **7**(11):699–712.
- Wei, Y., Wang, B., Wu, J., Yang, R., and Dunn, M. L. (2013). Bending rigidity and Gaussian bending stiffness of single-layered graphene. *Nano Lett.*, **13**(1):26–30.
- Wiberg, K. B. (1996). Bent bonds in organic compounds. *Acc. Chem. Res.*, **29**(5):229–234.
- Woodruff, S. R. and Filipov, E. T. (2020). Curved creases redistribute global bending stiffness in corrugations: theory and experimentation. *Meccanica*, **56**(6):1613–1634.
- Yang, S., Li, W., Ye, C., Wang, G., Tian, H., Zhu, C., He, P., Ding, G., Xie, X., Liu, Y., Lifshitz, Y., Lee, S.-T., Kang, Z., and Jiang, M. (2017). C3N—a 2D crystalline, hole-free, tunable-narrow-bandgap semiconductor with ferromagnetic properties. *Adv. Mater.*, **29**(16):1605625.
- Yu, L., Ruzsinszky, A., and Perdew, J. P. (2016). Bending two-dimensional materials to control charge localization and fermi-level shift. *Nano Lett.*, **16**(4):2444–2449.
- Zhang, D.-B., Akatyeva, E., and Dumitrică, T. (2011). Bending ultrathin graphene at the margins of continuum mechanics. *Phys. Rev. Lett.*, **106**(25):255503.
- Zhang, H.-Y. and Jiang, J.-W. (2015). Elastic bending modulus for single-layer black phosphorus. *J. Phys. D: Appl. Phys.*, **48**(45):455305.
- Zhang, T., Di, X., Chen, G., and Zhu, L. (2020). Parameterization of a COMPASS force field for single layer blue phosphorene. *Nanotechnology*, **31**(14):145702.
- Zhang, Z., Penev, E. S., and Yakobson, B. I. (2017). Two-dimensional boron: structures, properties and applications. *Chem. Soc. Rev.*, **46**(22):6746–6763.
- Zhao, J., Deng, Q., Ly, T. H., Han, G. H., Sandeep, G., and Rümmeli, M. H. (2015). Two-dimensional membrane as elastic shell with proof on the folds revealed by three-dimensional atomic mapping. *Nat. Commun.*, **6**(1):8935.